JCI insight

CD91 on dendritic cells governs immunosurveillance of nascent, emerging tumors

Abigail L. Sedlacek, … , Ion I. Mandoiu, Robert J. Binder

JCI Insight. 2019;4(7):e127239. https://doi.org/10.1172/jci.insight.127239.

Research Article Immunology

Graphical abstract

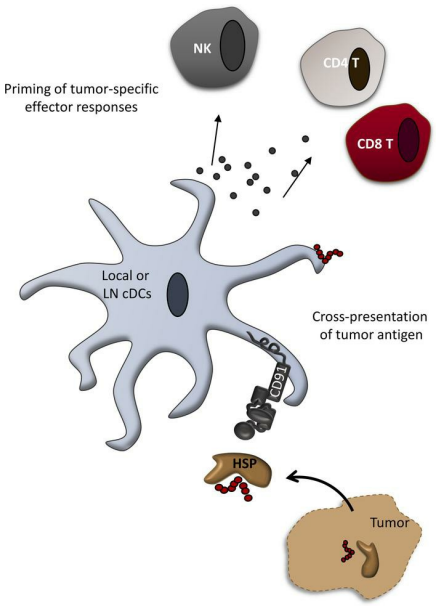

JCI insight

RESEARCH ARTICLE

CD91 on dendritic cells governs immunosurveillance of nascent, emerging tumors

Abigail L. Sedlacek,[1] Theodore P. Younker,[2] Yu Jerry Zhou,[3] Lisa Borghesi,[1] Tatiana Shcheglova,[4] Ion I. Mandoiu,[5] and Robert J. Binder[1]

[1]Department of Immunology, University of Pittsburgh, Pittsburgh, Pennsylvania, USA. [2]Institute for Health Metrics and Evaluation, University of Washington, Seattle, Washington, USA. [3]Targeted Therapeutics Discovery Unit, Pfizer, Pearl River, New York, USA. [4]Department of Immunology, University of Connecticut Health Center, Farmington, Connecticut, USA. [5]Department of Computer Science and Engineering, University of Connecticut, Storrs, Connecticut, USA.

The immune system detects aberrant, premalignant cells and eliminates them before the development of cancer. Immune cells, including T cells, have been shown to be critical components in eradicating these aberrant cells, and when absent in the host, incidence of cancer increases. Here, we show that CD91, a receptor expressed on antigen-presenting cells, is required for priming immune responses to nascent, emerging tumors. In the absence of CD91, effector immune responses are subdued, and tumor incidence and progression are amplified. We also show that, consequently, tumors that arise in the absence of CD91 express neo-epitopes with indices that are indicative of greater immunogenicity. Polymorphisms in human CD91 that are expected to affect ligand binding are shown to influence antitumor immune responses in cancer patients. This study presents a molecular mechanism for priming immune responses to nascent, emerging tumors that becomes a predictor of cancer susceptibility and progression.

Introduction

The observation that immune-compromised individuals are more susceptible to developing cancer has led to the current models of immunosurveillance (1, 2). $CD8^+$ T cells have been determined to be an immune effector population responsible for eliminating nascent, emerging tumors, thereby preventing cancer (3–5); in their absence, such as in *Rag*-deficient mice, multiple and frequent tumors emerge. Here we show that CD91, a receptor expressed on antigen-presenting cells (APCs), is similarly critical for efficient immunosurveillance of tumors.

The realization that most tumor rejection antigens are unique and derived from mutated proteins (6–9) predicts that the quantity of antigen available for cross-presentation in nascent, emerging tumors, is minute and is insufficient for cross-priming of T cell responses (10, 11) by current described pathways (12). Here we show that CD91 (13, 14) provides an essential and highly efficient conduit for cross-presentation of tumor antigens to T cells, and this pathway is necessary for mounting successful immune responses for surveillance of tumors. We found that mice lacking CD91 expression in DCs are more susceptible to development of chemically induced tumors compared with WT mice. Early effector immune responses were underdeveloped in these mice and enabled emergence of tumors expressing neo-antigens with a higher overall differential aggretope index. Furthermore, we show that polymorphisms in the CD91 gene that affect CD91-ligand interactions influence immune responses in patients with lung squamous cell carcinomas and skin cutaneous melanomas. Given that CD91 is also involved in activating NK cell responses (15), activating DCs to produce costimulation (16, 17), and priming T cells (17), our results begin to explain how effector immune responses to nascent, emerging tumors are developed.

Results

CD91 on DCs is necessary for antitumor immunity. Mice with a deficiency in CD91 expression in DCs ($CD91^{fl/fl}CD11c^{Cre}$) were created (Figure 1A), fully phenotyped, and had a normal hematopoietic compartment (18). $CD91^{fl/fl}CD11c^{Cre}$ mice or their controls ($CD91^{fl/fl}$) can generate normal Th1 responses

Conflict of interest: The authors have declared that no conflict of interest exists.

Submitted: January 7, 2019
Accepted: February 21, 2019
Published: April 4, 2019.

Reference information: *JCI Insight*. 2019;4(7):e127239. https://doi.org/10.1172/jci.insight.127239.

when immunized with a bolus of antigens in the form of peptides emulsified in complete Freund's adjuvant (18). The $CD91^{fl/fl}$ control mice (which are floxed but without Cre expression) are immunologically indistinguishable from C57BL/6 mice by all criteria we have tested, indicating the floxed CD91 gene by itself does not affect APCs. However, $CD91^{fl/fl}CD11c^{Cre}$ mice, and APCs derived from them, are deficient in cross-presentation (18) when antigen loads are low and, essentially, approaching physiological ranges. As a result, $CD91^{fl/fl}CD11c^{Cre}$ mice fail to mount Th1 immunity to implanted tumors, allowing tumors to grow at an enhanced rate compared with CD91-sufficient mice. Age-matched $CD91^{fl/fl}CD11c^{Cre}$ and $CD91^{fl/fl}$ mice were injected subcutaneously with 200 μg of methylcholantrene (MCA), a chemical carcinogen, and tumor development was monitored. $CD91^{fl/fl}CD11c^{Cre}$ mice developed tumors earlier than $CD91^{fl/fl}$ mice and with greater frequency ($P < 0.0004$). After 16 weeks, 85% of $CD91^{fl/fl}CD11c^{Cre}$ mice had developed tumors while only 20% of $CD91^{fl/fl}$ mice had tumors (Figure 1B). Immunodeficient mice with a targeted disruption of the recombination activating gene 2 (RAG2) lack B, T, and NKT cells and were incorporated into this experiment as a positive control. $Rag2^{-/-}$ mice developed tumors at the same time as $CD91^{fl/fl}CD11c^{Cre}$ mice, but tumor incidence was higher; 95% of $Rag2^{-/-}$ mice developed tumors by week 16. Tumors that formed in $CD91^{fl/fl}CD11c^{Cre}$ mice grew at a significantly faster rate than tumors in $CD91^{fl/fl}$ mice ($P < 0.0004$) (Figure 1C). Statistically, there was no difference in growth rate of tumors in $CD91^{fl/fl}CD11c^{Cre}$ versus $Rag2^{-/-}$ mice.

Immune effector responses are diminished in the absence of CD91. CD91 expressed on DCs is involved in activation of DCs and cross-priming of T cells (13–15, 19). We postulated that $CD91^{fl/fl}CD11c^{Cre}$ mice fail to mount sufficient immunity against the nascent, emerging tumors, hence the increased tumor incidence and enhanced growth compared with $CD91^{fl/fl}$ mice. We tested this by phenotyping the immune infiltrates in tumors that developed in $CD91^{fl/fl}$ and $CD91^{fl/fl}CD11c^{Cre}$ mice, with a focus on T cells and NK cells, which are the effectors responsible for tumor surveillance and which do not express CD91 (15). The analysis was performed on the earliest premalignant stage (at 2 weeks and before palpable tumors), after development of palpable tumors (9 weeks), and after development of late-stage tumors (18 weeks). $CD3^+$ cells infiltrating the site of pathology were significantly decreased at 2 weeks in $CD91^{fl/fl}CD11c^{Cre}$ mice compared with $CD91^{fl/fl}$ mice ($P < 0.05$) (Figure 2A). At this time point there was also a notable decrease in NK cells ($P = 0.059$) (Figure 2B). Even though this is a significant observation, the power of the data is, however, underrepresented because we noted that only a few of the $CD91^{fl/fl}$ mice (25%) went on to develop tumors compared with 85% of the $CD91^{fl/fl}CD11c^{Cre}$ mice (Figure 1). These differences were not observed at later time points when tumors were large and antigen dose was presumably greater (Figure 2, E, F, I, and J). We observed a significant decrease in the CD11b and CD11c (macrophage/DC) population in $CD91^{fl/fl}CD11c^{Cre}$ mice compared with $CD91^{fl/fl}$ mice at 2 weeks ($P < 0.05$) (Figure 2C), but not at 9 or 18 weeks (Figure 2, G and K), highlighting an additional role for CD91 in recruitment of APCs to the tumor site (20). No significant differences were observed in the $Gr1^+Ly6C^+$ populations, which would be inclusive of granulocytes at any examined time point (Figure 2, D, H, and L). Overall, there was no significant difference in total immune cell ($CD45^+$) or select lymphocyte ($CD3^+$ plus $NK1.1^+$) populations between the 2 groups at any time point (Figure 2, M and N). Flow cytometry data were also analyzed using the Cyt tool in MATLAB. L1 distance was used to calculate the difference in marker distribution between data sets for each time point in the 2 groups from MFI distribution plots. Distributions for the markers SSC, CD3, CD4, CD8, NK1.1, CD11b, Gr1, and Ly6C were analyzed within the entire $CD45^+$ population to determine any differences present in a system, which restricted experimenter bias. Samples from $CD91^{fl/fl}CD11c^{Cre}$ mice were set as the reference group, and changes were calculated based on the difference of the $CD91^{fl/fl}$ sample distribution from the $CD91^{fl/fl}CD11c^{Cre}$ samples. Positive L1 markers for cytotoxic cells (CD8, NK1.1) are confirmatory of differences between tumor infiltrates from $CD91^{fl/fl}CD11c^{Cre}$ and $CD91^{fl/fl}$ mice at the 2-week time point (Figure 2O). Interestingly, differential expression of Gr1 was observed between tumors from the 2 groups of mice, which is reflective of the granulocyte or myeloid derived suppressor cell (MDSC) population. These data exhibit the low effector immune populations present in tumors emerging in $CD91^{fl/fl}CD11c^{Cre}$ mice and suggest an additional role for CD91 in myeloid populations.

Tumors emerge and evolve with high antigenicity in the absence of CD91 on DCs. T cells exert their antitumor activity by recognizing tumor-specific antigens displayed by MHC molecules. Although many neo-antigens derived from somatic mutations can be identified in tumors, only a small subset of them serve as tumor rejection antigens. We examined neo-antigens arising in tumors in our study to qualify the neo-antigens responsible for rejection. Genomic DNA from tumors that arose each in $CD91^{fl/fl}CD11c^{Cre}$

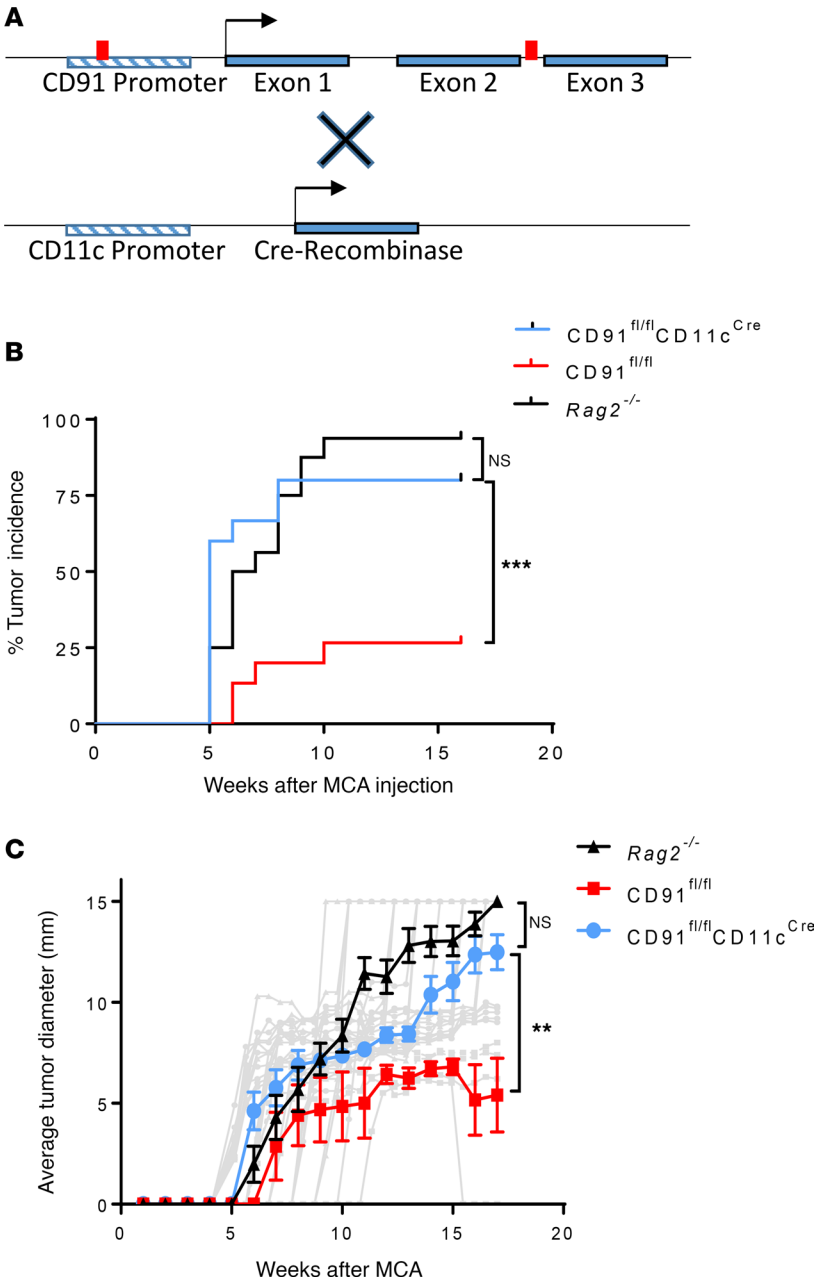

Figure 1. Lack of CD91 on DCs abrogates immunosurveillance of cancer. (**A**) Schematic for generating mice with a deficiency of CD91 in DCs. (**B**) Mice deficient in CD91 expression in CD11c cells ($CD91^{fl/fl}CD11c^{Cre}$, $n = 13$) were inoculated with a single dose of MCA s.c. WT littermates ($CD91^{fl/fl}$, $n = 15$) or *Rag2*$^{-/-}$ ($n = 15$) mice were similarly inoculated. Mice were monitored 3 times a week for the appearance of palpable tumors. Tumor incidence is identified as tumors greater than 2 mm in diameter in any axis. *P* values were obtained by Gehan-Breslow-Wilcoxon text. (**C**) Tumors that grew in any mice ($n = 11$, 4, and 14 for $CD91^{fl/fl}CD11c^{Cre}$, $CD91^{fl/fl}$, and *Rag2*$^{-/-}$ mice, respectively) were measured. Growth curves for individual mice are shown in gray with the same group symbol. *P* values were obtained by 1-way ANOVA analysis of comparisons of area under the curve for each group. $^{**}P < 0.01$, $^{***}P < 0.001$.

($n = 6$) or $CD91^{fl/fl}$ ($n = 7$) mice were obtained and libraries prepared and subjected to whole-exome sequencing (Supplemental Table 1; supplemental material available online with this article; https://doi.org/10.1172/jci.insight.127239DS1). No differences in the total number of single nucleotide variations (SNVs) between the 2 groups were observed (Figure 3A). For each nonsynonymous somatic mutation, we used NetMHC 4.0 to compute the predicted binding affinity of each 8-, 9-, 10-, and 11-mer–mutated peptide for the H-2-K^b and H-2-D^b alleles (with amino acids flanking the mutation). There was no difference in total number of predicted mutated peptides between the 2 groups (Figure 3B).

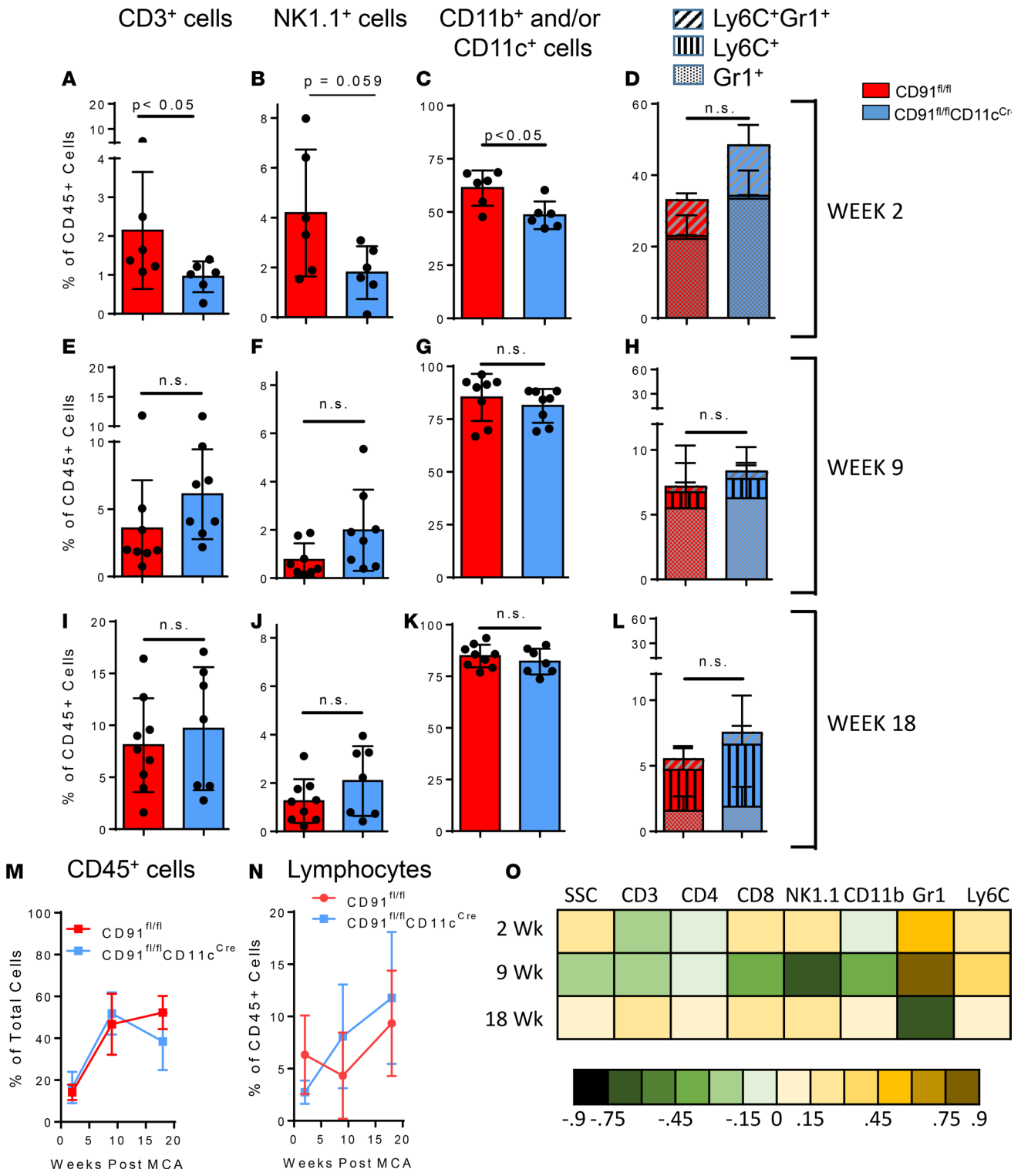

Figure 2. Lack of CD91 on DCs prevents priming of effector responses to emerging tumors. Mice were injected with 200 μg MCA s.c. The injection site was harvested 2 weeks later (**A**–**D** and **M**–**O**) or the palpable tumor 9 and 18 weeks later (**E**–**L** and **M**–**O**) and analyzed by flow cytometry. Frequencies of $CD3^+$ cells (**A**, **E**, and **I**), $CD3^-NK1.1^+$ cells (**B**, **F**, and **J**), and $CD11b^+$ and $CD11c^+$ cells (**C**, **G**, and **K**) were measured. (**D**, **H**, and **L**) Remaining $CD11b^-CD11c^-$ cells were further separated into populations that were either $Ly6C^+$ or $Gr1^+$. Each circle represents samples from a single mouse. The error bars depict standard deviation. The bar predicts the median. The length of the box represents the interquartile range. (**M** and **N**) The frequency of leukocytes ($CD45^+$ cells) within the tumor was determined at each time point (**M**), as well as the frequency of lymphocytes ($CD3^+$ and $NK1.1^+$) among the $CD45^+$ cells (**N**). (**O**) Flow cytometry (FCS) data were analyzed via unsupervised approaches using the MATLAB tool Cyt. The L1 statistical differences between the MFI distribution of the indicated markers on $CD45^+$ cells were determined. The data are reported so that distributions derived from $CD91^{fl/fl}CD11c^{Cre}$ mice are the reference population, and the difference calculated is the change in the $CD91^{fl/fl}$ mice distribution from the reference. Analyses were done on $n = 6$ mice/group, and statistical significance was determined by Student's 2-tailed t test.

We then classified mutated peptides according to IC_{50} as high binders (IC_{50} < 500), poor binders (IC_{50} < 1000), or unlikely binders (IC_{50} < 5000) to MHC as measured in vitro. We observed no differences in the number of mutant peptides from $CD91^{fl/fl}CD11c^{Cre}$ mouse– or $CD91^{fl/fl}$ mouse–derived tumors at any threshold of IC_{50} (Figure 3, C–E). These data suggest that immune recognition of nascent tumors was not based on peptides with in vitro defined high affinity for MHC I, called the classically defined neo-epitopes, as is routinely done (21). This observation held true when we separated the peptides into individual D^b and K^b alleles (data not shown).

Differential aggretope index (DAI) is a measure of the differential binding affinity between the WT and corresponding mutated peptides and has emerged as a vital determinant for T cell recognition of novel cancer neo-peptides and identification of tumor rejection antigens (22). Mutant peptides with high DAI are targeted by T cell immunity, leading to tumor rejection (22–24). The average DAI for D^b and K^b binding peptides was significantly higher in the $CD91^{fl/fl}CD11c^{Cre}$-derived tumors compared with $CD91^{fl/fl}$-derived tumors (Figure 3F). The difference in DAI between the 2 groups was not present when only high-affinity peptides (IC_{50} < 500) were analyzed (Figure 3G), indicating that many poor binders (IC_{50} > 500) were being targeted by the immune system and in fact may be the mutated peptide population that is most responsible for tumor surveillance. Mutant peptides were then ranked according to their DAI for association with D^b and K^b. Tumors that developed in $CD91^{fl/fl}CD11c^{Cre}$ mice expressed significantly more mutated peptides with a DAI greater than 7 than tumors from $CD91^{fl/fl}$ mice (Figure 3H). This difference was not present in mutated peptides with DAI less than 7. To confirm the evolution of tumors with high DAI in $CD91^{fl/fl}CD11c^{Cre}$ ($H\text{-}2^b$) mice, we examined DAI for the same mutated peptides in association with unexpressed $H\text{-}2^d$ alleles. There was no difference in DAI between tumors that developed in $CD91^{fl/fl}$ or $CD91^{fl/fl}CD11c^{Cre}$ mice when association of mutated peptides with D^d or K^d MHC alleles was examined (Figure 3I). These results show that T cells survey emerging tumors by targeting neo-antigens with high DAI, and not necessarily by targeting neo-antigens that bind expressed MHC with high affinity, and eliminate these tumors. In CD91-deficient mice, a lack of infiltrating T cells allows tumors expressing neo-antigens with higher DAI to emerge.

Polymorphisms in CD91 influence immunity and cancer progression. Given the importance of CD91 in immunosurveillance of tumors in our murine model and the better overall survival of advanced melanoma patients with high CD91 expression in monocytes (25), we postulated that SNVs in human CD91 that affect ligand (HSP) binding could modulate cross-presentation of tumor neo-antigens, cross-priming T cell responses and thus the overall effector immune response to tumors. We constructed an in silico analysis pipeline combining several tools allowing for mass testing of large volumes of publicly available SNV data to predict novel SNVs with high impact on CD91 binding by immunogenic HSPs. We harvested 24,101 human SNVs from National Center for Biotechnology Information (NCBI) dbSNP and filtered for exonal missense SNVs resulting in amino acid mutations that were physiochemically different from WT. Our criteria produced 1233 candidate SNVs distributed across all 89 exons of the CD91 protein sequence (Figure 4A). Candidate SNVs were further processed through 2 independent deleterious prediction algorithms, SIFT and PolyPhen2, to predict SNV impact on protein product stability and function. Of these, 402 "high-impact" SNVs were predicted to be deleterious or damaging by both algorithms, with 250 SNVs located in ligand binding domains (I-IV) and 300 SNVs residing in inter–binding domain spaces (2–3, 3–4, and 4 to C-terminus) (Supplemental Table 2). All SNVs were individually incorporated into CD91 amino acid sequences and sent through a stability change prediction meta-server, iStable, to determine their influence on CD91 structure (Supplemental Table 2). Large changes in ΔΔG value depict high impact (negative and positive values representing increased or decreased stability, respectively) on stability of CD91 compared with WT. All ΔΔG stability values were normalized to enable cross-region comparison, and results were visualized using R packages ggplot2 and manhattanly (Figure 4B). Multiple SNVs were shown to have significant predicted impact on CD91 stability.

Next, we modeled docking of the immunogenic HSP paralogs, gp96 and hsp90, with CD91 in the presence or absence of individual SNVs residing in ligand binding domains. Several high-impact SNVs were captured that significantly increased or decreased the fold change in docking energy of CD91 with HSP (Figure 4C). No overlap was observed between the SNVs predicted for large ΔΔG impact on CD91 stability (Figure 4B) and those SNVs predicted for large ΔΔG impact on HSP-CD91 docking (Supplemental Figure 1); thus ΔΔG docking energy for each SNV will have to be individually determined for other CD91 ligands that are immunogenic (14, 26).

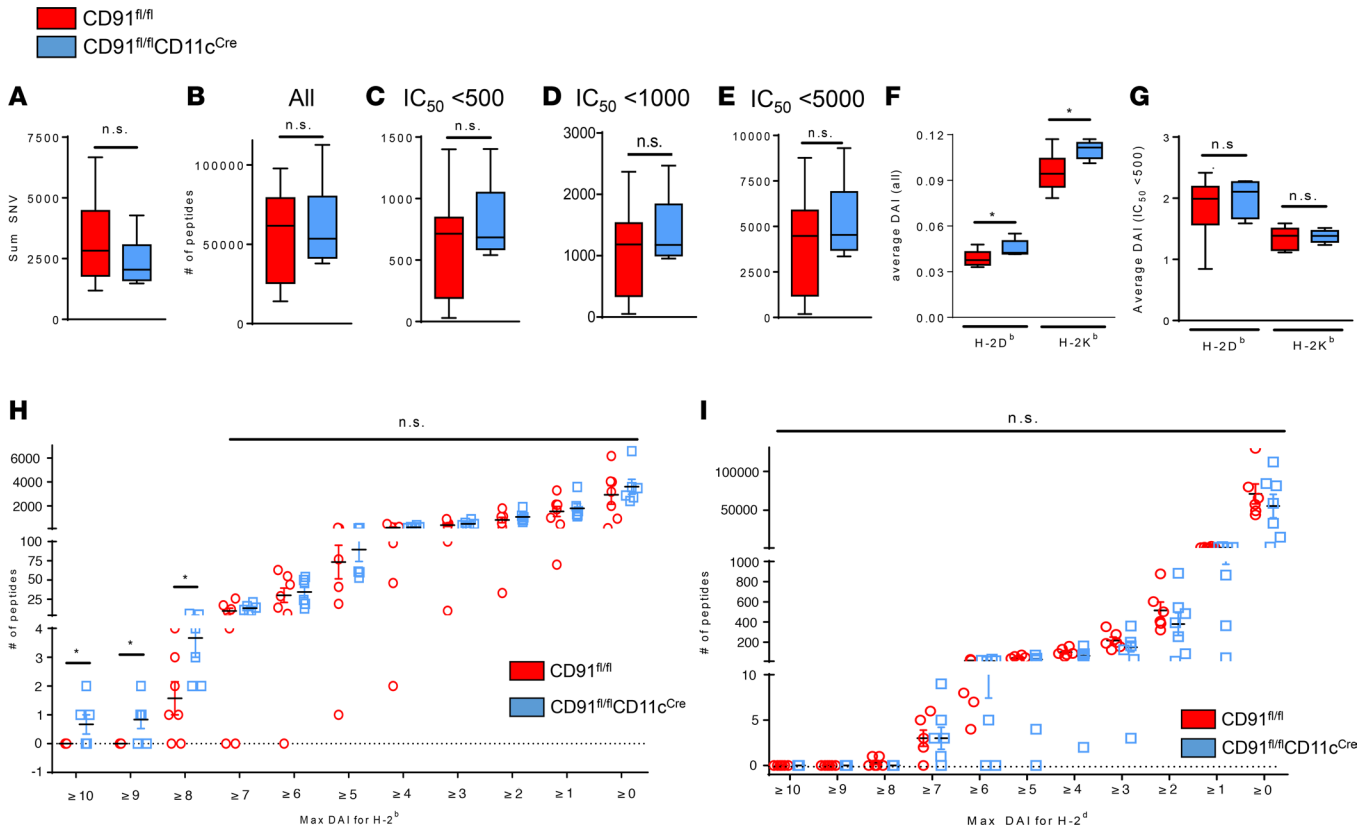

Figure 3. CD91-mediated immunity to nascent tumors is fixated on neo-epitopes with high differential aggretope index. Tumors induced with MCA in CD91$^{fl/fl}$CD11c^{Cre} and CD91$^{fl/fl}$ mice were harvested and analyzed by whole-exome sequencing. (**A**) Total number of all SNVs derived from tumors in either group. (**B**) The total number of 8-, 9-, 10-, and 11-mer–mutated peptides spanning the mutation and predicted from each SNV. (**C**–**E**) The number of mutated peptides with the indicated half maximal inhibitory concentration (IC_{50}) threshold. (**F**) The average differential aggretope index (DAI), which measures the differential binding affinity between the WT and corresponding mutated peptides, derived from all mutated peptides for the H-2-K^b or H-2-D^b MHC allele. (**G**) The average DAI for only mutated peptides with high affinity for H-2-K^b or H-2-D^b MHC binding (IC_{50} < 500). The box plots depict the minimum and maximum values (whiskers), the upper and lower quartiles, and the median. The length of the box represents the interquartile range. (**H** and **I**) The number of peptides with indicated maximum DAI for H-2^b (**H**) or H-2^d (**I**). Statistical significance was determined by Student's 2-tailed *t* test. *P < 0.05.

We examined patient samples deposited in the Genomic Data Common (GDC) portal for the presence of CD91 SNV and its impact on CD8$^+$ T cell representation in tumors as measured by RNA sequencing (RNA-Seq). We first analyzed patients with lung squamous cell carcinoma. CD91 SNVs at positions 105, 639, 2623, and 3504 (black arrows in Figure 4C) that had a high-impact +/–ΔΔG docking to HSP appeared individually in 4 patients. SNV 105 had a +ΔΔG docking impact (worse binding to HSP) while SNVs 639, 2623, and 3504 had –ΔΔG docking impact (better binding to HSP). Patients with a –ΔΔG (SNVs 639, 2623, and 3504) had higher CD8$^+$ T cell infiltrates in their tumors (average fragments per kilobase of transcript per million mapped reads [FPKM] = 15.4) compared with the patient with a +ΔΔG (SNV 105), who had low CD8$^+$ T cell infiltrates (FPKM = 1.3) (Figure 4D). We next examined additional CD91 SNVs with high +/–ΔΔG docking impact that were found in patients with skin cutaneous melanoma (red arrows in Figure 4C). SNVs at positions 539, 978, and 3581 (all –ΔΔG) correlated with increased levels of CD8$^+$ T cells found in tumors (average FPKM = 2.48) compared with the patient tumor with +ΔΔG (SNV 3308, FPKM = 0.1) (Figure 4E). However, a patient outlier (SNV 978) was observed, with –ΔΔG but no observable increase in CD8$^+$ T cell tumor infiltrate, adding weight to the importance of additional factors that influence T cell infiltration.

Discussion

The direct and comprehensive implication of CD91 in immunosurveillance of nascent, emerging tumors yielded several important conclusions. First, T cell recognition of nascent tumors occurs via neo-antigen peptides with the highest DAI in association with expressed MHC I. These peptides are the tumor rejection antigens (22), are unique to each tumor, and are not necessarily those with highest MHC-binding affinity as

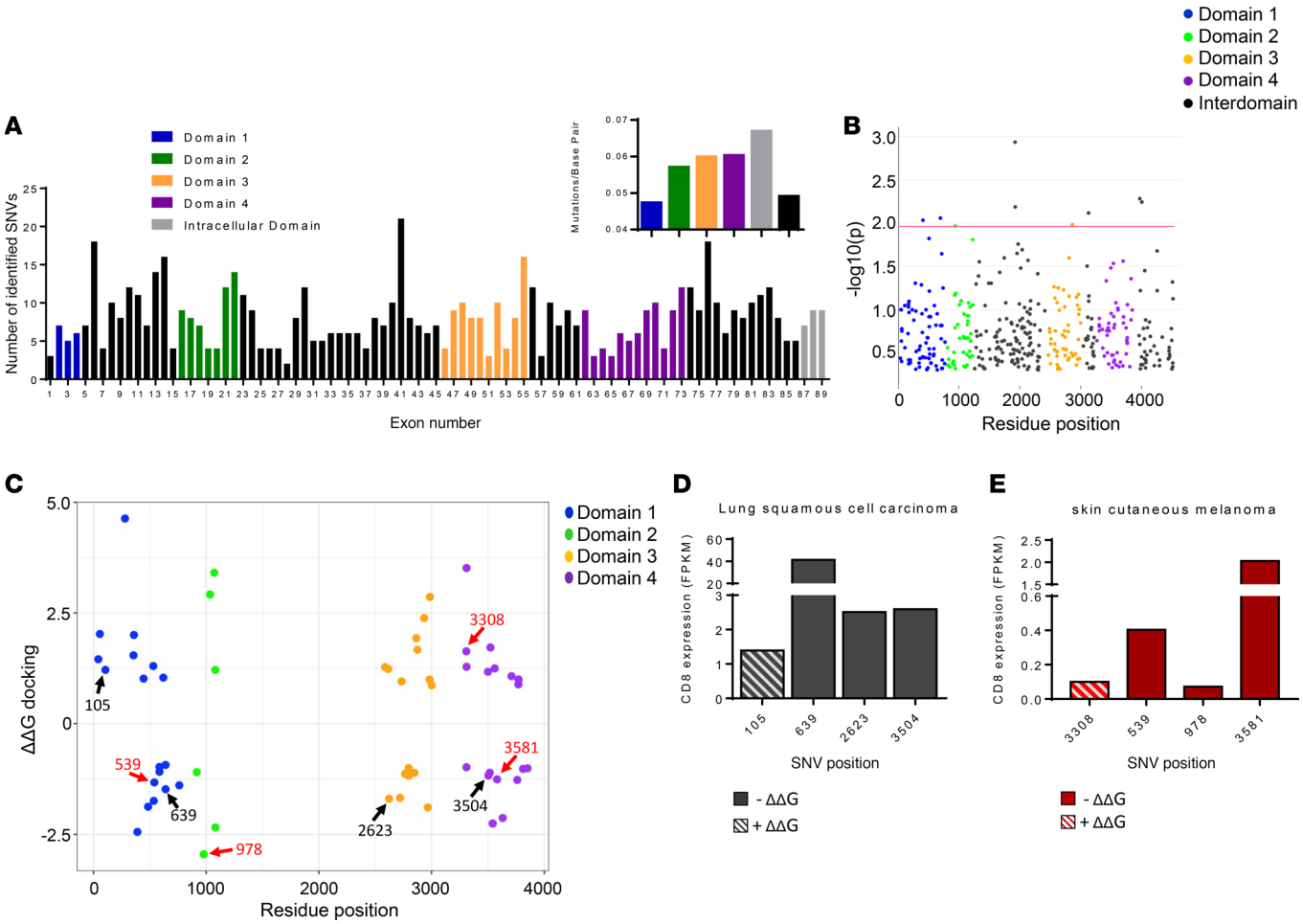

Figure 4. Effect of predicted high-impact SNVs on receptor stability, HSP docking, and antitumor effector response. (**A**) Distribution of 1233 candidate SNVs binned into 89 exons of the CD91/LRP1 gene. Individual ligand binding domains are indicated. Interdomain regions that play no binding or membrane anchoring role are colored uniformly black. The inset figure shows the number of mutations per base in each domain. Vertical height of each bar indicates the number of SNPs falling within that exon. (**B**) Visualization of high-impact SNV –log(*P* value) score of change in stability energy between the SNV-altered CD91 and WT. Higher scores represent increased magnitude of change in stability energy compared with all other candidate SNVs. Red line was chosen at a Z score of 1.96, and points above this threshold have a $P < 0.05$. (**C**) Scatter plot of high-impact SNV effect on hsp90-CD91 binding interactions. Negative and positive scores represent increased binding or decreased ligand binding, respectively, in hsp90-altered CD91 receptors compared with WT reference binding energies. The 4 ligand binding domains of CD91 are color coded as indicated. Black arrows represent SNVs that appear in 4 individual patients with lung squamous cell carcinoma, and red arrows represent SNVs that appear in 4 individual patients with skin cutaneous melanoma. The position of each SNV is indicated by a number next to each arrow. (**D** and **E**) Stacked bar plot showing predicted high-impact SNVs in human samples of lung squamous cell carcinomas (**D**) or skin cutaneous melanoma (**E**) and the associated presence of $CD8^+$ immune cells from transcriptomic data. RNA-Seq expression levels (in FPKM) are used as a proxy for $CD8^+$ T cell presence. Solid bars indicate SNVs with –ΔΔG docking impact, and hatched bars indicate SNVs with +ΔΔG docking impact.

currently defined by in vitro methods. In the absence of CD91, which prevents DCs from cross-presenting HSP-chaperoned peptides (13, 14, 19), tumors with high DAI emerge. The current definition of what constitutes an immunologically relevant tumor rejection antigen is mired in assigning an IC_{50} score to neo-epitopes, which is based on an in vitro competition assay of peptide binding to MHC (27). As discussed elsewhere, there are numerous deficiencies and exceptions to this definition both in mouse models of cancer and in the clinical setting (28). It is therefore not surprising that we observe no immunological selection of neo-epitopes based on the IC_{50} score at any cutoff. Rather we observe immune selection centered on those epitopes exhibiting a high DAI, an index that has emerged as a more accurate predictor of tumor rejection antigens (22–24). Second, cross-priming of immune responses by HSP-chaperoned peptide complexes released from tumor cells attends to 2 conundrums of the current immunosurveillance model; first, the efficiency of cross-presentation of antigens through the HSP-CD91 pathway addresses the vast disparity in antigen amount used in previously described cross-presentation systems and that which occurs in nascent tumors in vivo (10, 11), at early time points of tumorigenesis when T cell responses can be easily measurable (29–31). The second conclusion

is that T cell responses require costimulation for priming, and HSPs are capable of providing signals for T cell costimulation through CD91 (16, 17). Our previous work with $CD91^{fl/fl}CD11c^{Cre}$ mice showed the role of tumor-derived HSP in priming $CD8^+$ T cell responses to *implanted* tumors (18). That system allowed the subtle titration of antigen dose available for cross-priming. The HSP-CD91 pathway was shown to be required for antitumor immunity when antigen in a few thousand tumor cells was present, which is in the range of the prepalpable (week 2), MCA-induced tumors developed here. Our findings of decreased $CD8^+$ T cells and NK cell infiltrates in CD91-deficient mice at early time points (Figure 2) are therefore fully consistent with the inability of tumor-derived HSP to prime and activate these cells, respectively (15, 18). The third conclusion is that CD91 SNVs that occur within the human population have the potential to affect HSP ligand binding. By analyzing The Cancer Genome Atlas (TCGA) data for patients with lung squamous cell carcinomas and skin cutaneous melanoma, we identified several of these SNV that are detrimental to HSP binding. These occur in the ligand binding domains of CD91 and resulted in a poorer immune response as measured by fewer tumor infiltrating $CD8^+$ T cells. We also found SNV with converse effects on HSP binding and patients with these had higher numbers of tumor infiltrating CD8 cells. Narrowing down the cumulative effects of all SNV on an individual scale is becoming important since effects on binding affinities of each SNV within a single gene may cancel out or enhance another. In concert with CD91 SNVs, early observations indicate that CD91 expression levels may likewise be important for developing antitumor immunity (25). In this regard, high CD91 expression in APCs confers a better prognosis in patients with advanced melanoma. The dual factors of CD91 SNV and expression levels will be a critical determinant in priming immune responses that influence the genesis and progression of cancer. Additional roles for CD91 beyond cross-presentation of HSP-chaperoned antigens are also under consideration (20). Given the requirement of pre-existing T cell responses for successful check-point blockade cancer monotherapy (32–34), deficiencies in CD91 function, either by SNV or insufficient expression levels will be a major determining factor for such treatments, overall prognosis for disease progression, and also for identifying individuals at risk for developing cancer.

Methods

Mice. Female C57BL/6, B6(Cg)-$Rag2^{tm1.1Cgn}$/J (*Rag2*$^{-/-}$ C57BL/6), mice (catalog 008449) were purchased from The Jackson Laboratory. $CD91^{fl/fl}CD11c^{Cre}$ and $CD91^{fl/fl}$ littermates have been previously described. All mice were housed or bred in the animal facility at the University of Pittsburgh (Pittsburgh, Pennsylvania, USA). All experimental mice were 6 to 8 weeks old. All experiments with mice were approved by the Institutional Animal Care and Use Committee at the University of Pittsburgh and performed in compliance with its guidelines.

Tumor induction and immune phenotyping. Tumors were induced in mice by intradermal injection of 200 μg of MCA (MilliporeSigma) dissolved in peanut oil (MilliporeSigma). The injection site (at week 2) and palpable tumor (at weeks 9 and 18) were harvested as indicated in figures. Tissue was immediately mechanically disrupted, followed by enzymatic digestion using 0.2% Collagenase D (MilliporeSigma) in RPMI and 2% BSA (MilliporeSigma). Cell suspensions were stained for flow cytometry in PBS with 1% BSA and 0.1% sodium azide using the following antibodies from BD Biosciences — α-CD45.2 (catalog 560695), α-CD4 (catalog 550954), α-CD8α (catalog 558106), α-NK1.1 (catalog 564144), α-CD11b (catalog 553312), α-CD11c (catalog 564986), and α-Gr1 (catalog 557979) — or eBiosciences — α-CD3e (catalog 11-0031-85) and α-Ly6C (catalog 48-5932-80). Cells were acquired by flow cytometry on a BD LSRII and analyzed using FlowJo software (Tree Star Inc.). FCS data were also analyzed via unsupervised approaches using the MATLAB tool Cyt (35).

Exome sequencing. Genomic DNA from tumors of size 10- to 12-mm diameter was purified using the Qiagen Puregene Kit. The Genomic DNA was sheared with Ion Shear Plus Reagents (Ion Plus Fragment Library Kit) and size selected with Agencourt AMPure XP beads (Beckman Coulter). DNA fragments with a bp peak of 100–150 bp were ligated with Ion adapters, purified with Agencourt AMPure XP beads, and PCR amplified. Then, 750 ng of the adapter-ligated DNA library was hybridized to SureSelect capture library (Agilent SureSelect XT Mouse All Exon Kit) for 20 hours at 65°C. The hybrid capture library was selected using Dynabeads MyOne Streptavidin T1 beads (Life Technologies). The captured library was amplified and purified with AMPureXP beads, and quality was assessed on the High Sensitivity DNA Kit (Life Technologies) on the Agilent Bioanalyzer. We selected 220-bp peak using E-Gel SizeSelect 2% agarose gel (Life Technologies). The final library was purified and quality assessed on High Sensitivity DNA Bioanalyzer chip (Life Technologies). Templates were prepared using the Ion PI Hi-Q Chef Kit (Life Technologies) on the Ion Chef platform and sequenced on an Ion Proton Sequencer on a PI v3 chip using Ion PI Hi-Q Sequencing 200 Kit (Life Technologies).

Prediction of neo-epitopes. Exome reads were mapped against mm10 reference genome using the HISAT2 version 2.1.0 alignment program (36) with options "--sensitive --no-discordant --no-mixed --no-unal." SNVs were called using the SNVQ tool included in the NGSTools package version 2.0.0 (37). SNVQ computes posterior probabilities for each possible genotype based on quality scores of aligned bases and calls a variant if the genotype with highest posterior probability is not a homozygous reference. High-confidence SNVs were selected by requiring a genotype Phred score of 50 and a minimum of 3 reads supporting the alternative allele, with at least 1 read mapping on each strand. Heterozygous SNVs unique to each tumor were classified as novel somatic mutations. Homozygous SNVs as well as heterozygous SNVs shared by more than 1 tumor were considered germline mutations and were not used for epitope prediction. Prediction of neo-epitopes was performed based on Consensus CDS annotations release 16 (38) using a custom Galaxy tool. For each nonsynonymous somatic mutation, we used NetMHC 4.0 (39) to compute the predicted binding affinity (IC_{50}) of each 8-, 9-, 10-, and 11-mer–mutated peptide for the H-2-K^b and H-2-D^b alleles.

CD91 SNP mining. All available SNPs were mined from the NCBI's dbSNP (https://www.ncbi.nlm.nih.gov/snp). Filters were applied to select for significant missense SNPs. These were aligned to the human LRP1 FASTA mRNA nucleotide sequence (NM_002332.2) obtained from NCBI's Nucleotide database (https://www.ncbi.nlm.nih.gov/nuccore). Resultant nucleotide changes were then translated to the corresponding LRP1 amino acid sequence obtained from the Universal Protein Resource Knowledgebase (http://www.uniprot.org/). The final data set was automatically organized to contain information for the number of the amino acid residue changed (e.g., residue 32), the relative number of the residue within that domain's generated 3D model (e.g., residue 14 in binding domain 1), the codon allele (e.g., T or G) change, and the residue change (e.g., F to L). Using this data set, SNP-specific LRP1 FASTA amino acid sequences were created for each candidate missense SNP. FASTA amino acid sequences for binding domains 1, 2, 3, and 4, along with the interdomain space between binding domains 2 and 3, 3 and 4, and 4 and C-terminus ending. These were used as input for computational 3D modeling.

CD91 domain modeling. The LRP1 receptor is large and therefore prohibitive for traditional structure determination techniques, such as NMR or crystallography, with less than 4% of the protein structure available in Research Collaboratory for Structural Bioinformatics Protein Data Bank (https://www.rcsb.org/). Therefore, we used a divide-and-conquer strategy by generating 3D structures for WT binding domains 1, 2, 3, and 4 as well as interdomain spaces 2–3, 3–4, and 4 to C-terminus ending. Unique 3D models were created for all candidate SNPs integrated into their respective domains. We generated models using I-TASSER prediction server (40). To ensure an optimal final model, all generated models were refined using ModRefiner (41). Model visualization was performed through PyMol (The PyMOL Molecular Graphics System, Version 1.2r3pre, Schrödinger, LLC).

Deleterious CD91 SNV prediction. All candidate SNVs were first submitted to SIFT to predict SNV-caused amino acid substitutions' effect on protein function based on amino acid conversation rate across species (42). All candidate SNVs were then submitted to PolyPhen2 to predict effect of SNV-caused amino acid substitution on both function and structure based on sequence alignment and probabilistic machine learning classification (43). Both tools serve as a dual algorithmic measure of deleterious impact of individual SNVs.

Prediction of SNP impact on CD91 stability. SNP-induced changes in CD91 stability were determined using iStable (44). This web-based tool is an integrated stability predictor that uses a combination of protein sequence and structure information as input to produce a meta-result backed by a support vector machine trained on 6 popular prediction tools. Results from I-Mutant 2.0 were used to provide a quantitative prediction of SNP-induced stability change based on the same input used previously with iStable (45).

Prediction of SNP impact on CD91 hsp90 docking affinity. Docking simulations were performed for all 3D models of WT CD91 ligand binding domains and all SNV-specific 3D models. All receptor models were paired with human hsp90 serving as the docking ligand. Simulations were run using Hex Protein Docking, an interactive docking program that allows for efficient simulation of multiparameter large-molecule docking aided by graphics processing unit acceleration (46). The calculated $\Delta\Delta G$ values reflect the degree of impact an SNV has on the docking energy of HSP-CD91 binding interactions compared to WT CD91, with negative and positive values representing increased or decreased binding affinity, respectively. All $\Delta\Delta G$ docking values were normalized to enable cross–binding domain comparison, and results were combined into a final data set with predicted impact, stability scores, and docking scores (Supplemental Table 2).

Data processing and figure construction. Programming languages for harvesting and filtering SNVs was done in Java with accessory shell scripting for task automation. Macros were constructed using Java and implemented to automate docking simulations. Data analysis of candidate SNVs and visualization of results were

performed in R with the aid of ggplot/plotly/webshot packages for figure creation and tidyverse, dplyr, data.tibble, reshape2, and magrittr packages for data transformations. Plots using GDC-deposited TCGA data were created using data harvested from the NIH National Cancer Institute Genomic Data Commons Data Portal (https://portal.gdc.cancer.gov/). All cancer samples containing relevant CD91 SNVs were collected manually. Transcriptome data in RNA-Seq FPKM format (Supplemental Table 3) were used to elucidate the relative presence of immune cell infiltrate in tumors via presence of immune cell–specific marker genes in a given sample. Immune cell–specific marker gene symbols were identified by keyword search with their corresponding Ensembl gene stable IDs, retrieved through Ensembl Biomart (http://useast.ensembl.org/index.html).

Statistics. Statistical analysis was run using GraphPad Prism software version 7. Student's 2-tailed *t* test or area under the curve followed by 1-way ANOVA were used where indicated in the figure legends. Figure 1B was analyzed by Gehan-Breslow-Wilcoxon test. *P* less than 0.05 was considered significant.

Study approval. All experiments with mice were approved by the Institutional Animal Care and Use Committee at the University of Pittsburgh and performed in compliance with its guidelines.

Author contributions

ALS, YJZ, and RJB performed and analyzed data from the tumor induction experiments. ALS performed the flow cytometry analysis. TS analyzed the tumor SNV and neo-epitope prediction pipeline. LB contributed to the Flow cytometry analysis. TPY and RJB performed the bioinformatics analysis of CD91 SNV and GDC-deposited TCGA data. TS and IIM performed the genomic analysis on tumors. RJB planned the research. All authors contributed to data interpretation and discussion of results.

Acknowledgments

We thank Anupinder Kaur and Adam Hagymasi (University of Connecticut Health Center) for tumor exome sequencing. We acknowledge support from NIH CA208833 (to RJB), NIH 1S10OD011925-01 (to LB), and NIH AI126440 (to LB).

Address correspondence to: Robert J. Binder, University of Pittsburgh School of Medicine, E1058 Biomedical Science Tower, 200 Lothrop St., University of Pittsburgh, Pittsburgh, Pennsylvania 15261, USA. Phone: 412.383.7722; Email: rjb42@pitt.edu.

1. Birkeland SA, et al. Cancer risk after renal transplantation in the Nordic countries, 1964-1986. *Int J Cancer*. 1995;60(2):183–189.
2. Chen DS, Mellman I. Oncology meets immunology: the cancer-immunity cycle. *Immunity*. 2013;39(1):1–10.
3. Svane IM, Engel AM, Nielsen MB, Ljunggren HG, Rygaard J, Werdelin O. Chemically induced sarcomas from nude mice are more immunogenic than similar sarcomas from congenic normal mice. *Eur J Immunol*. 1996;26(8):1844–1850.
4. Matsushita H, et al. Cancer exome analysis reveals a T-cell-dependent mechanism of cancer immunoediting. *Nature*. 2012;482(7385):400–404.
5. Johnson L, et al. Somatic activation of the K-ras oncogene causes early onset lung cancer in mice. *Nature*. 2001;410(6832):1111–1116.
6. Schumacher TN, Schreiber RD. Neoantigens in cancer immunotherapy. *Science*. 2015;348(6230):69–74.
7. Srivastava PK. Neoepitopes of cancers: looking back, looking ahead. *Cancer Immunol Res*. 2015;3(9):969–977.
8. Delamarre L, Mellman I, Yadav M. Cancer immunotherapy. Neo approaches to cancer vaccines. *Science*. 2015;348(6236):760–761.
9. Srivastava PK. Do human cancers express shared protective antigens? or the necessity of remembrance of things past. *Semin Immunol*. 1996;8(5):295–302.
10. Li M, et al. Cell-associated ovalbumin is cross-presented much more efficiently than soluble ovalbumin in vivo. *J Immunol*. 2001;166(10):6099–6103.
11. Binder RJ, Srivastava PK. Peptides chaperoned by heat-shock proteins are a necessary and sufficient source of antigen in the cross-priming of $CD8^+$ T cells. *Nat Immunol*. 2005;6(6):593–599.
12. Grotzke JE, Sengupta D, Lu Q, Cresswell P. The ongoing saga of the mechanism(s) of MHC class I-restricted cross-presentation. *Curr Opin Immunol*. 2017;46:89–96.
13. Binder RJ, Han DK, Srivastava PK. CD91: a receptor for heat shock protein gp96. *Nat Immunol*. 2000;1(2):151–155.
14. Basu S, Binder RJ, Ramalingam T, Srivastava PK. CD91 is a common receptor for heat shock proteins gp96, hsp90, hsp70, and calreticulin. *Immunity*. 2001;14(3):303–313.
15. Sedlacek AL, Kinner-Bibeau LB, Binder RJ. Phenotypically distinct helper NK cells are required for gp96-mediated anti-tumor immunity. *Sci Rep*. 2016;6:29889.
16. Basu S, Binder RJ, Suto R, Anderson KM, Srivastava PK. Necrotic but not apoptotic cell death releases heat shock proteins, which deliver a partial maturation signal to dendritic cells and activate the NF-kappa B pathway. *Int Immunol*. 2000;12(11):1539–1546.
17. Pawaria S, Binder RJ. CD91-dependent programming of T-helper cell responses following heat shock protein immunization. *Nat Commun*. 2011;2:521.
18. Zhou YJ, Messmer MN, Binder RJ. Establishment of tumor-associated immunity requires interaction of heat shock proteins with CD91. *Cancer Immunol Res*. 2014;2(3):217–228.

19. Binder RJ, Srivastava PK. Essential role of CD91 in re-presentation of gp96-chaperoned peptides. *Proc Natl Acad Sci U S A*. 2004;101(16):6128–6133.
20. Staudt ND, et al. Myeloid cell receptor LRP1/CD91 regulates monocyte recruitment and angiogenesis in tumors. *Cancer Res*. 2013;73(13):3902–3912.
21. Van Allen EM, et al. Genomic correlates of response to CTLA-4 blockade in metastatic melanoma. *Science*. 2015;350(6257):207–211.
22. Duan F, et al. Genomic and bioinformatic profiling of mutational neoepitopes reveals new rules to predict anticancer immunogenicity. *J Exp Med*. 2014;211(11):2231–2248.
23. Rech AJ, et al. Tumor immunity and survival as a function of alternative neopeptides in human cancer. *Cancer Immunol Res*. 2018;6(3):276–287.
24. Ghorani E, et al. Differential binding affinity of mutated peptides for MHC class I is a predictor of survival in advanced lung cancer and melanoma. *Ann Oncol*. 2018;29(1):271–279.
25. Stebbing J, et al. The common heat shock protein receptor CD91 is up-regulated on monocytes of advanced melanoma slow progressors. *Clin Exp Immunol*. 2004;138(2):312–316.
26. Binder RJ, Karimeddini D, Srivastava PK. Adjuvanticity of alpha 2-macroglobulin, an independent ligand for the heat shock protein receptor CD91. *J Immunol*. 2001;166(8):4968–4972.
27. Sette A, et al. Peptide binding to the most frequent HLA-A class I alleles measured by quantitative molecular binding assays. *Mol Immunol*. 1994;31(11):813–822.
28. Brennick CA, George MM, Corwin WL, Srivastava PK, Ebrahimi-Nik H. Neoepitopes as cancer immunotherapy targets: key challenges and opportunities. *Immunotherapy*. 2017;9(4):361–371.
29. Nasti TH, et al. Immunoprevention of chemical carcinogenesis through early recognition of oncogene mutations. *J Immunol*. 2015;194(6):2683–2695.
30. North RJ. The murine antitumor immune response and its therapeutic manipulation. *Adv Immunol*. 1984;35:89–155.
31. North RJ, Kirstein DP. T-cell-mediated concomitant immunity to syngeneic tumors. I. Activated macrophages as the expressors of nonspecific immunity to unrelated tumors and bacterial parasites. *J Exp Med*. 1977;145(2):275–292.
32. Topalian SL, et al. Safety, activity, and immune correlates of anti-PD-1 antibody in cancer. *N Engl J Med*. 2012;366(26):2443–2454.
33. Brahmer JR, et al. Safety and activity of anti-PD-L1 antibody in patients with advanced cancer. *N Engl J Med*. 2012;366(26):2455–2465.
34. Sharma P, Allison JP. The future of immune checkpoint therapy. *Science*. 2015;348(6230):56–61.
35. Amir el-AD, et al. viSNE enables visualization of high dimensional single-cell data and reveals phenotypic heterogeneity of leukemia. *Nat Biotechnol*. 2013;31(6):545–552.
36. Kim D, Langmead B, Salzberg SL. HISAT: a fast spliced aligner with low memory requirements. *Nat Methods*. 2015;12(4):357–360.
37. Duitama J, Srivastava PK, Măndoiu II. Towards accurate detection and genotyping of expressed variants from whole transcriptome sequencing data. *BMC Genomics*. 2012;13 Suppl 2:S6.
38. Pruitt KD, et al. The consensus coding sequence (CCDS) project: Identifying a common protein-coding gene set for the human and mouse genomes. *Genome Res*. 2009;19(7):1316–1323.
39. Andreatta M, Nielsen M. Gapped sequence alignment using artificial neural networks: application to the MHC class I system. *Bioinformatics*. 2016;32(4):511–517.
40. Zhang Y. I-TASSER server for protein 3D structure prediction. *BMC Bioinformatics*. 2008;9:40.
41. Xu D, Zhang Y. Improving the physical realism and structural accuracy of protein models by a two-step atomic-level energy minimization. *Biophys J*. 2011;101(10):2525–2534.
42. Kumar P, Henikoff S, Ng PC. Predicting the effects of coding non-synonymous variants on protein function using the SIFT algorithm. *Nat Protoc*. 2009;4(7):1073–1081.
43. Adzhubei IA, et al. A method and server for predicting damaging missense mutations. *Nat Methods*. 2010;7(4):248–249.
44. Chen CW, Lin J, Chu YW. iStable: off-the-shelf predictor integration for predicting protein stability changes. *BMC Bioinformatics*. 2013;14 Suppl 2:S5.
45. Capriotti E, Fariselli P, Casadio R. I-Mutant2.0: predicting stability changes upon mutation from the protein sequence or structure. *Nucleic Acids Res*. 2005;33(Web Server issue):W306–W310.
46. Macindoe G, Mavridis L, Venkatraman V, Devignes MD, Ritchie DW. HexServer: an FFT-based protein docking server powered by graphics processors. *Nucleic Acids Res*. 2010;38(Web Server issue):W445–W449.